IEEE Open Journal of
Power Electronics

Received 13 August 2023; revised 17 September 2023; accepted 20 September 2023. Date of publication 26 September 2023; date of current version 11 October 2023. The review of this paper was arranged by Associate Editor Hang Dai.

Digital Object Identifier 10.1109/OJPEL.2023.3319488

An Optimal Control Strategy for the DAB-Based Partial Power Converter Based on Extended-Phase-Shift Control

SHANSHAN GAO [1] (Member, IEEE), YIXUE ZHANG [1], YIJIE WANG [1] (Senior Member, IEEE), JIANXING LIU [2] (Senior Member, IEEE), AND DIANGUO XU [1] (Fellow, IEEE)

[1]School of Electrical Engineering and Automation, Harbin Institute of Technology, Harbin 150001, China
[2]Department of Control Science and Engineering, Harbin Institute of Technology, Harbin 150001, China

CORRESPONDING AUTHOR: SHANSHAN GAO (e-mail: gaoshanshan@hit.edu.cn)

This work was supported in part by the National Natural Science Foundation of China under Grant 52207194, and in part by the Heilongjiang Province Postdoctoral Science Foundation under Grant LBH-Z22023.

ABSTRACT Dual active bridge (DAB) converters are extensively used due to the advantages of wide voltage regulation range and easy realization of soft switching. Besides, the concept of partial power converters (PPCs) has been widely applied to increase the converter efficiency by reducing the power actually processed by the converter. Therefore, in this article, the DAB converter and PPC are combined. And a high frequency DAB-based PPC aiming at efficiency optimization is selected out by analyzing and comparing the characteristics of several connections. Considering the wide voltage regulation range of DAB-based PPC, the extended-phase-shift-based control strategy aiming at zero-voltage switching (ZVS) range and current stress optimization is analyzed and adopted in this article. With the trend of high frequency for power converters, the non-ideal factors like output capacitors of switches need to be considered to improve the performance. The output capacitors are taken into consideration when analyzing the ZVS performance and the magnetizing inductor is utilized to expand ZVS range. To verify correctness of theoretical analysis, a prototype using GaN devices with 1 kW rated output power and 500 kHz switching frequency is built. The experimental results are consistent with the analysis.

INDEX TERMS Extended-phase-shift control, DAB converters, partial power converters, switch output capacitors.

I. INTRODUCTION

DAB converters are widely applied in photovoltaic (PV), electric vehicles (EVs), energy storage systems (ESSs), and DC distribution due to the advantages of bidirectional power transmission, symmetrical structure, high power density, and easy realization of soft switching [1], [2], [3], [4], [5]. High frequency is one of the most popular trends of power converters. Higher operation frequency can make passive components such as transformers and inductors smaller, which can increase the power density and reduce the cost. However, with the increase of the switching frequency, the switching loss becomes a serious problem under the condition of hard switching, which can cause EMI aggravation, efficiency decrease and more heat produce [6], [7], [8]. Therefore, the achievement of ZVS is a crucial factor for converters to get better performance under the condition of high frequency.

For DAB converters, the realization of ZVS has to do with the control method. Phase-shift control is commonly used in DAB converters. Single-phase-shift (SPS) control is a classical method which is easy to be implemented because there is only one phase-shift angle between the two H-bridges [1]. When the gain equals to one, DAB converters can achieve full load range ZVS of all switches under SPS control. However, when the gain deviates from one, the current stress and backflow power will increase, and ZVS will lose, which will lead to efficiency decrease [9]. To improve the performance, many control strategies with multiple phase-shift angles are proposed, such as extended-phase-shift

(EPS) control [10], dual-phase-shift (DPS) control [11] and triple-phase-shift (TPS) control [12].

As for EPS control, besides the phase-shift angle similar with that in SPS control, which is defined as the outer phase-shift angle, there is a phase difference between the switches on diagonal line of one of the two H-bridges, which is defined as the inner phase-shift angle. This is the difference between the two control strategies. Benefited from the additional phase-shift angle, the current stress and reactive power decrease and the ZVS region expands, which can improve the efficiency [11], [13]. DPS control and EPS control are similar, but the difference is that in DPS, the switch pairs on diagonal lines of the two H-bridges have the same inner phase-shift angles. TPS control makes the same inner phase-shift angles of DPS control independent. For control strategies with multiple degrees of freedom, there are various combinations of phase-shift angles to realize different optimization goals, such as expanding ZVS range [14], [15], minimizing current stress [16], minimizing backflow power [17], [18], enhancing light-load performance [19], [20], and minimizing root-mean-square (RMS) current [21], [22].

Under the condition of high frequency, the effects of the output capacitors of switches can be amplified because the charging and discharging process of output capacitors are hard to be ignored due to short switching period. For DAB converters, the achievement of ZVS in essence is that the resonant network formed by the output capacitors and the auxiliary inductor finishes the discharging process of output capacitors of the switches before the driving signals come [23]. Thus, the output capacitors of switches should be taken into account when analyzing ZVS conditions.

Current stress is an important performance metric of DAB converters. For DAB converters, the current stress is the maximum value of the auxiliary inductor current. Low current stress can bring low cost, low loss and high reliability. A control strategy aiming at optimization of current stress and ZVS range is proposed in [24], but the parasitic parameters are not taken into account, and it is hard to be implemented due to the high control complexity made by excessive degrees of freedom. In [25], the effects of nonideal factors including output capacitors and dead time are analyzed at length and a control strategy is proposed to achieve soft switching in a wide range as far as possible without considering current stress optimization. Furthermore, the ZVS regions are seamed, which causes non-ZVS realization in the transition of operation modes.

To improve the efficiency further for large power applications, PPCs have gain more and more attention recent years due to the advantages of increasing power density and efficiency, which are realized by directly establishing an additional power path from input side to output side [26], [27]. PPCs have been effectively applied in PV [28], EVs [29], and ESSs [30], which is highly overlapped with the applications of DAB converters. Therefore, the combination of PPCs and DAB converters has been widely applied [30], [32]. The efficiency of partial power converters is up to 98.22% in [28], 99.11% in [29], 98.2% in [30] and 99.6% in [31]. The reason of such high-level efficiencies is that most of the energy is transmitted through the direct path while only the rest fractional energy is processed by the converters. The efficiency of the energy directly transmitted approximately equals to 1. Thus, compared to conventional full power converters, PPCs have smaller size and higher efficiency due to less energy processed in practice.

TABLE 1. Relationships of V_i, I_i, V_o and I_o

Connection	V_i	I_i	V_o	I_o
1	V_1-V_2	I_2	V_1	I_2-I_1
2	V_1-V_2	I_1	V_2	I_2-I_1
3	V_1	I_1-I_2	V_1-V_2	$-I_2$
4	V_2	I_1-I_2	V_1-V_2	$-I_1$

In this article, a DAB-based PPC is selected and adopted, which increases the efficiency by an additional energy path. All the connection methods are analyzed and compared to pick out the most efficient path. And the effects of output capacitors under EPS control are analyzed in detail for better high frequency performance, which make two ZVS regions separate from each other. To make the regions continuous, the magnetizing inductance is considered. The magnetizing inductance can expand the ZVS regions and its constraint conditions are analyzed. Finally, an EPS-based control strategy aiming at reducing current stress and full load range ZVS is analyzed and applied. In addition, Gallium nitride (GaN) devices with faster turn-on/off speed are applied to make dead time shorter compared to silicon devices [33], [34], which can avoid dead-time effects to a certain extent.

This article is organized as follows. In Section II, four common partial power connections are analyzed, and the most appropriate connection is selected. Then the DAB-based PPC are combined according to the analysis. In Section III, the effects of output capacitors and magnetizing current under EPS control are analyzed in detail. In Section IV, the control strategy aiming at optimization of ZVS range and current stress considering output capacitors and magnetizing inductor is analyzed. Sections V and VI give the analysis of the experimental results and conclusion respectively.

II. SELECTION OF PARTIAL POWER CONVERTER TOPOLOGY

Partial power processing is to establish a direct connection between input side and output side of converters. The direct connection methods can affect the performance of PPCs. There are four common connection methods as shown in Fig. 1. V_1, I_1, V_2 and I_2 are the voltages and currents of input side and output side of the system, respectively. The input and output voltages and currents of the internal converter cell are defined as V_i, I_i, V_o and I_o, respectively. The relationships between the above parameters are summarized in Table 1.

This article focuses on EV applications, therefore, the input voltage $V_1 = 400$ V, the output voltage $V_2 = 300$ V

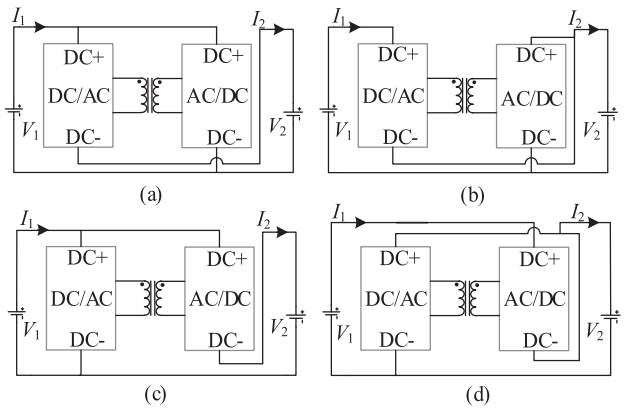

FIGURE 1. Four common connections of partial power converters. (a) Connection 1. (b) Connection 2. (c) Connection 3. (d) Connection 4.

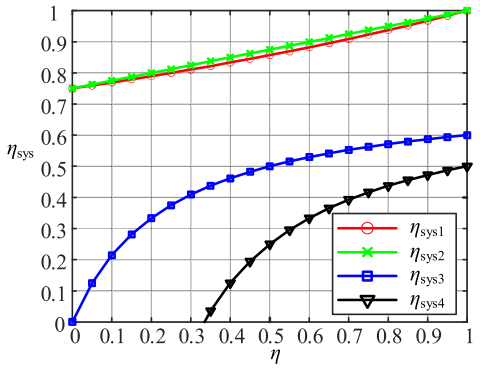

FIGURE 2. Efficiency curves of the four common connections.

and the rated power is 1 kW. To select the most appropriate connection, the four connections in Fig. 1 are analyzed and compared with the traditional full power converter. Assuming the efficiency of the converter is η, the efficiency of the full power system can be calculated as:

$$\eta = \frac{V_2 I_2}{V_1 I_1} \tag{1}$$

The system efficiencies of the above four connections are calculated as follows:

$$\eta_{sys1} = \frac{V_2}{(1-\eta)V_1 + \eta V_2} \tag{2}$$

$$\eta_{sys2} = \frac{\eta V_1 + (1-\eta)V_2}{V_1} \tag{3}$$

$$\eta_{sys3} = \frac{\eta V_2}{(\eta+1)V_1 - V_2} \tag{4}$$

$$\eta_{sys4} = \frac{(\eta+1)V_1 - V_2}{\eta V_1} \tag{5}$$

where η_{sys1}, η_{sys2}, η_{sys3}, η_{sys4} are the efficiencies of the connection 1, 2, 3 and 4, respectively.

According to the above equations, the efficiency curves of the four systems as shown in Fig. 2 can be obtained. With

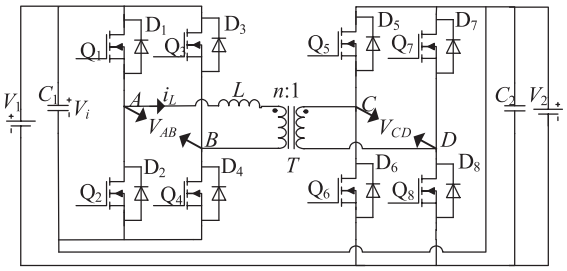

FIGURE 3. DAB-based PPC topology.

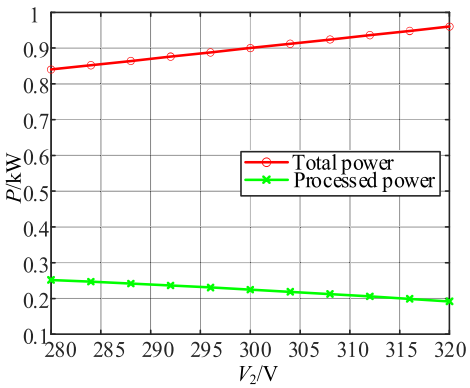

FIGURE 4. Power curves with different output voltage.

the increase of η, the efficiencies of the four systems increase, and it can be seen that η_{sys2} is the highest in the whole range of η. Therefore, the connection 2 in Fig. 1(b) is adopted in this article with the consideration of efficiency. Therefore, the topology of the DAB-based PPC is determined as shown in Fig. 3. The direct path from input side to output side has been added to the DAB converter. Similarly, V_1 and V_2 are the input voltage and the output voltage of the system. The actual input voltage of the DAB converter is V_i. And it is apparent that $V_i = V_1 - V_2$. The transformer turn ratio is defined as n. $k = V_i / nV_2$ is defined as the voltage conversion ratio of the converter. The output voltages of primary and secondary H bridges are V_{AB} and V_{CD}, respectively. The current of L is i_L. The switching frequency is f and the duty cycle is T.

When the output current of the converter keeps 0.3A, the curves of the total power and power actually processed by the DAB converter with different output voltages are shown in Fig. 4. It can be concluded that the when the output voltage increases, the actual processed power deceases, which is beneficial to decrease the size and cost of the converter. However, there are some disadvantages for the DAB-based PPC. For conventional DAB converters, the more input and output voltages match, the better performance can be achieved. Nevertheless, for DAB-based PPC, the more input and output voltages match, though this brings less processed power, the more the voltage gain of the internal DAB cell deviates from one due to the input voltage $V_i = V_1 - V_2$. Therefore, for the DAB-based PPC, the internal DAB cell has a wider voltage

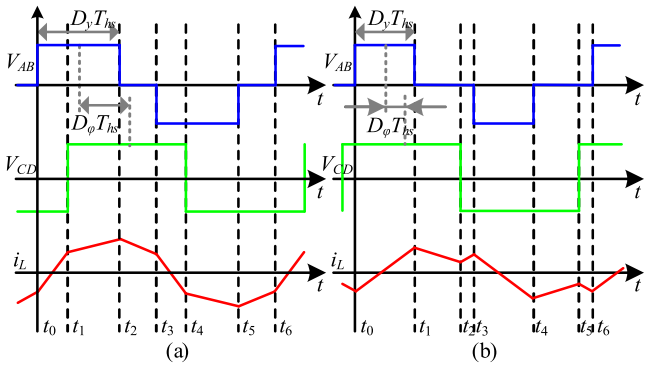

FIGURE 5. Key waveforms under EPS control. (a) Mode A. (b) Mode B.

regulation range than the conventional DAB converter, which means another appropriate control is needed to be implemented instead of the SPS control.

III. ANALYSIS OF FULL LOAD RANGE ZVS OPTIMIZATION BASED ON EPS CONTROL

As mentioned above, although SPS control is easy to be implemented, its voltage regulation range is narrow. When the voltage gain deviates from one, the ZVS range is limited and current stress increases, which is led by the single degree of freedom. Compared to SPS control, EPS control can achieve better performance when the gain is not one by two degrees of freedom, which is not complicated to be implemented. According to the analysis in Section II, the internal DAB cell of the PPC has a wider voltage regulation range compared to traditional DAB converters. Therefore, EPS control is applied in the following analysis.

A. DEFINITION OF NEW MODES

The normalized transmission power expression under EPS control is derived as:

$$p = \begin{cases} 2\left(-D_1^2 + 2D_1D_2 - D_1 - 2D_2^2 + 2D_2\right) & D_1 \le D_2 \\ 4\left(D_2 - \frac{1}{2}D_1\right)(1 - D_1) & D_2 < D_1 \end{cases} \tag{6}$$

where the inner phase-shift ratio D_1 is the ratio of inner phase-shift angle of the primary H-bridge to π, and outer-phase-shift ratio D_2 is the ratio of outer phase-shift angle to π.

In order to simplify the calculation, the new outer-shift ratio is defined as $D_\varphi = D_2$ - D_1 / 2 and the new inner-shift ratio is defined as $D_y = 1$ - D_1. Under the new definitions of the phase-shift ratios, the new modes are redefined according to the edge and position of the waveforms of V_{AB} and V_{CD}. There are three modes under the new definitions. The range of phase-shift ratios of mode A, mode B and mode C are $0.5(1 - D_y) \le D_\varphi \le 0.5(1 + D_y)$, $0 \le D_\varphi \le 0.5(1 - D_y)$ and $0.5(1 + D_y) \le D_\varphi \le 1$ respectively. There will be a large circulating current if $D_\varphi > 0.5$, hence only the first two modes are actually applied. Thus, only the mode A and B are analyzed, and the upper limit of mode A is forced to be 0.5. The key waveforms of the two modes are shown in Fig. 5.

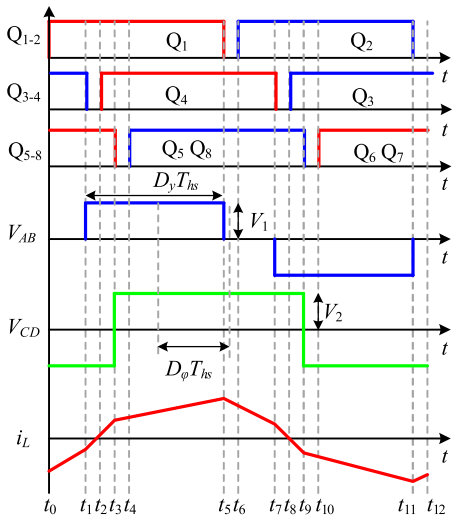

FIGURE 6. Waveforms under EPS control considering output capacitors.

According to (6), the new expressions of the normalized transmission power can be obtained as follows:

$$\begin{cases} p_A = -4D_\varphi^2 - D_y^2 + 4D_\varphi + 2D_y - 1 \\ p_B = 4D_yD_\varphi \end{cases} \tag{7}$$

where p_A and p_B are the transmission power of mode A and mode B.

B. CONDITIONS OF ZVS CONSIDERING OUTPUT CAPACITORS

Take mode A for example, the conditions of ZVS are analyzed. The output capacitors are taken into account to make the ZVS conditions more precise under high switching frequency. Fig. 6 shows the waveforms of mode A under EPS control with the consideration of the output capacitors. The i_L is calculated as:

$$i_L(t) = \begin{cases} -\frac{nV_2}{4fL}\left[(k-1)D_y + 2D_\varphi\right] & t = t_0 \\ -\frac{nV_2}{4fL}\left[(k+1)D_y + 2\left(D_\varphi - 1\right)\right] & t = t_1 \\ -\frac{nV_2}{4fL}\left(k - 1 - 2kD_\varphi\right) & t = t_3 \\ -\frac{nV_2}{4fL}\left[(1-k)D_y + 2D_\varphi\right] & t = t_5 \end{cases} \tag{8}$$

Fig. 7 shows the equivalent circuits of the charging/discharging process of mode A. C_s is the output capacitor of the switch. Similarly, i_{Cs} is the current of the output capacitor. To simplify the analysis, the values of all output capacitors are same. Only the case of $k > 1$ is analyzed, which is similar to the case of $k < 1$.

At t_1, Q_3 turns off. As shown in Fig. 7(a), i_L discharges the output capacitor of Q_4, in the meantime, it charges the output capacitor of Q_3. The end of the charging/discharging process is defined as t_{m1}. From t_1 to t_{m1}, i_L can be derived as :

$$i_L(t) = C_s\frac{du_{Cs4}}{dt} - C_s\frac{du_{Cs3}}{dt} = -2C_s\frac{du_{Cs3}}{dt} \tag{9}$$

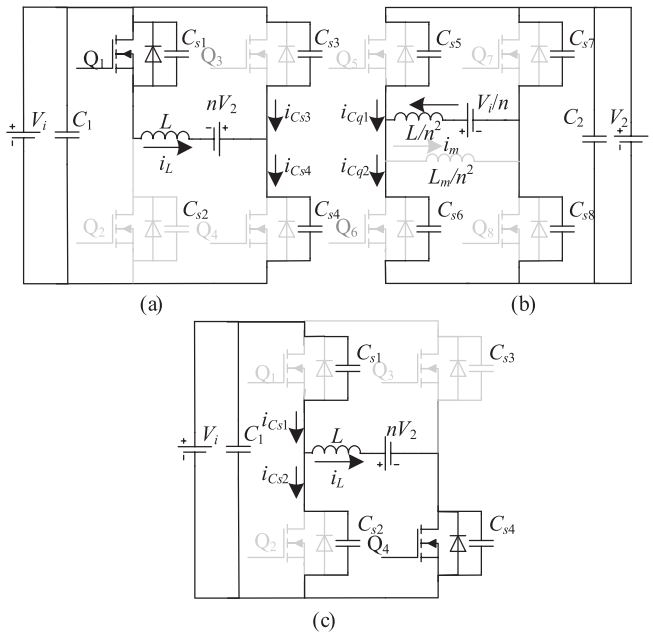

FIGURE 7. Equivalent ZVS circuit of mode A. (a) t_1 – t_2. (b) t_3 - t_4. (c) t_5 - t_6.

According to the energy conservation, the energy relationship can be obtained as:

$$E_{t_1} = E_{t_m} + E_{\text{loss}} + E_{\text{del}} \tag{10}$$

where E_{t1} and E_{tm} are the energy stored by the inductor L at t_1 and t_m, respectively. E_{del} is the energy transmitted by L. E_{loss} is the energy loss.

In this process, it can be equivalently regarded as that the energy of Q_4 is transmitted to Q_3 through L meanwhile some energy of the primary side is transmitted to the secondary side through L. Regardless of the power loss, E_{del1} is the energy transmitted by the inductor current, which can be calculated as:

$$\begin{aligned} E_{\text{del1}} &= E_{t_1} - E_{t_m} \\ &= \int_{t_1}^{t_{m1}} \left[-nV_2 i_L(t) - V_i i_{Cs4}(t)\right] \mathrm{d}t \\ &= C_s V_i^2 \left(1 + \frac{2}{k}\right) \end{aligned} \tag{11}$$

The relationship of the energy E stored in the inductor L and the current I of L is as follows:

$$E = \frac{1}{2} L I^2 \tag{12}$$

According to (11) and (12), the expression of I_{min} which is the minimum inductor current to ensure ZVS achievement is derived as:

$$I_{\text{min}} = \sqrt{2C_s V_i^2 \left(1 + \frac{2}{k}\right) \frac{1}{L}} \tag{13}$$

Therefore, the ZVS condition of Q_3 and Q_4 is obtained as :

$$i_L(t_1) \le -V_i \sqrt{2C_s \left(1 + \frac{2}{k}\right) \frac{1}{L}} \tag{14}$$

Further, the ZVS condition expressed by D_y and D_φ is calculated as:

$$D_y \ge \frac{2\left(1 - D_\varphi\right) + a\sqrt{\left(k^2 + 2k\right)}}{1 + k} \tag{15}$$

where $a = (32LC_s)^{0.5}/T$.

At t_3, Q_6 and Q_7 turn off. As shown in Fig. 7(b), i_s is the current of the secondary side, it discharges the output capacitors of Q_5 and Q_8, meanwhile, it charges the output capacitors of Q_6 and Q_7 from t_3 to t_4. The magnetizing inductor is neglected here. The output capacitors of secondary side and the equivalent inductor form the resonant network, which means the energy keeps unchanged. The condition of ZVS of Q_5 and Q_8 is derived as:

$$i_s(t_3) = n i_L(t_3) \ge 0 \tag{16}$$

At t_5, Q_1 turns off. As shown in Fig. 7(c), i_L discharges the output capacitor of Q_2 while it charges the output capacitor of Q_1. In this process, the charging/discharging end point is defined as t_{m2}. The expressions of i_L and the energy are as:

$$i_L(t) = C_s \frac{du_{Cs1}}{dt} - C_s \frac{du_{Cs2}}{dt} = 2C_s \frac{du_{Cs1}}{dt} \tag{17}$$

$$E_{\text{del2}} = \int_{t_1}^{t_{m2}} \left[nV_2 i_L(t) - V_i i_{Cs1}(t)\right] \mathrm{d}t = C_s V_i^2 \left(\frac{2}{k} - 1\right) \tag{18}$$

Therefore, the ZVS conditions of Q_2 are calculated as:

$$\begin{cases} i_L(t_5) \ge 0 & k > 2 \\ i_L(t_5) \ge V_i \sqrt{2C_s \left(\frac{2}{k} - 1\right) \frac{1}{L}} & 1 < k \le 2 \end{cases} \tag{19}$$

Similarly, the expression of the ratios are calculated as:

$$\begin{cases} D_y \ge \frac{a\sqrt{(2k-k^2)} - 2D_\varphi}{k-1} & k \le 2 \\ D_y \ge \frac{-2D_\varphi}{k-1} & k > 2 \end{cases} \tag{20}$$

The mode B ZVS conditions of all switches can be analyzed and obtained similarly. The ZVS conditions of all switches in the two modes are summarized in Table 2. It can be concluded that the ZVS conditions are stricter and more complicated when taking output capacitors into consideration.

Fig. 8 shows the C_s influence on ZVS region in detail. Fig. 8(a) shows the change trend of ZVS region with the increase of C_s. Fig. 8(b), (c) and (d) show the ZVS regions under the condition of $k = 1.33$ with 0pF, 65pF and 200pF capacitances respectively, wherein the 65pF is the output capacitance of GS66508B which is the switch adopted in this article. It can be seen that due to the output capacitors, the ZVS region is divided into two parts. With the increase of the output capacitance, the degree of the separation increases, and the non-ZVS-realization power range expands.

TABLE 2. ZVS Conditions of All Switches

Switches	ZVS conditions of mode A	ZVS conditions of mode B
Q_5-Q_8	$D_\varphi \geq \frac{1}{2}\left(1-\frac{1}{k}\right)$	$D_y \leq \frac{1}{k}$
Q_3-Q_4	$D_y \geq \frac{2\left(1-D_\varphi\right)+a\sqrt{\left(k^2+2k\right)}}{1+k}$	$\begin{cases} D_y \geq \frac{2D_\varphi+a\sqrt{\left(k^2-2k\right)}}{k-1} & k \geq 2 \\ D_y \geq \frac{2D_\varphi}{k-1} & k < 2 \end{cases}$
Q_1-Q_2	$\begin{cases} D_y \geq \frac{a\sqrt{\left(2k-k^2\right)}-2D_\varphi}{k-1} & k \leq 2 \\ D_y \geq \frac{-2D_\varphi}{k-1} & k > 2 \end{cases}$	$\begin{cases} D_y \geq \frac{a\sqrt{\left(2k-k^2\right)}-2D_\varphi}{k-1} & k \leq 2 \\ D_y \geq \frac{-2D_\varphi}{k-1} & k > 2 \end{cases}$

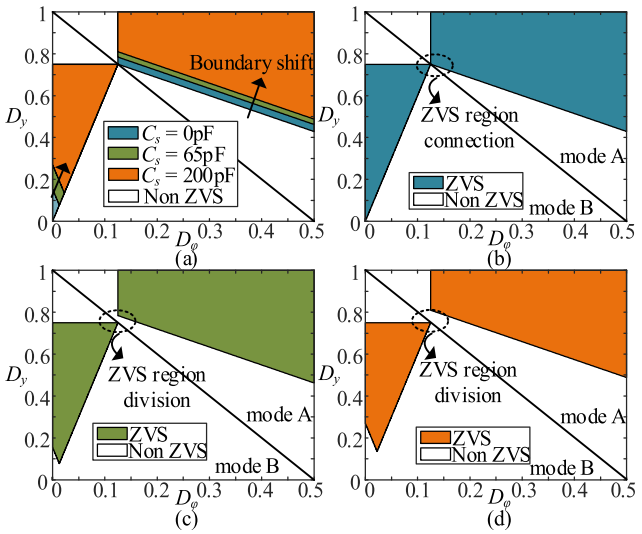

FIGURE 8. ZVS regions of all switches with output capacitance consideration. (a) ZVS region comparison. (b) ZVS region with 0pF output capacitance. (c) ZVS region with 65pF output capacitance. (d) ZVS region with 200pF output capacitance.

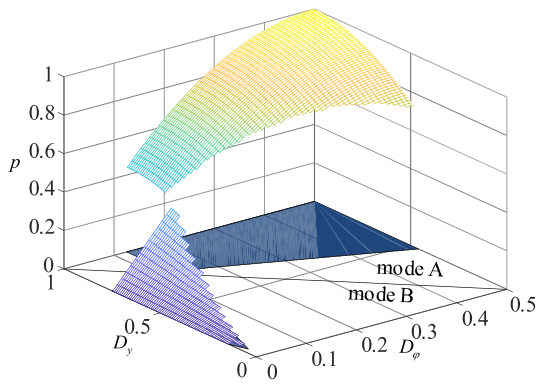

FIGURE 9. Power transfer surface in the ZVS regions with 65pF output capacitance.

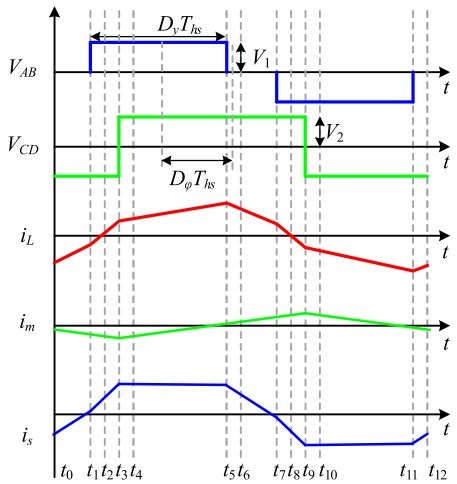

FIGURE 10. Main waveforms considering the magnetizing current i_m.

Fig. 9 shows the transmission power surface in the ZVS region with 65pF output capacitance. It can be seen that due to the separation of the ZVS region, the power surface is divided into two parts. In the gap between the parts, ZVS cannot be realized, which means the ZVS realization is not ensured in the whole power range.

C. CONSTRAINT CONDITIONS OF MAGNETIZING INDUCTOR

To make the two separate ZVS regions connected, the magnetizing current is taken into consideration, which can expand the ZVS region. As shown in Fig. 10, the magnetizing current i_m influences i_s, but the waveform of i_L remains constant.

The expression of i_s is as follows:

$$i_s(t) = n\left[i_L(t) - i_m(t)\right] \tag{21}$$

Because of the change of i_s, the conditions of ZVS also change. Therefore, the secondary side current limit of mode A is derived as:

$$i_s(t_3) = n\left[i_L(t_3) - i_m(t_3)\right] \geq 0 \tag{22}$$

Due to the symmetry of the magnetizing current, the magnetizing current at t_3 is calculated as:

$$i_m(t_3) = -\frac{nV_2}{4fL_m} \tag{23}$$

Further, the ZVS condition of Q_5-Q_8 in mode A is obtained as:

$$D_\varphi \geq \frac{1}{2}\left[1-\frac{1}{k}\left(1+\frac{L}{L_m}\right)\right] \tag{24}$$

Similarly, the ZVS condition of Q_5-Q_8 in mode B is as follows:

$$D_y \leq \frac{1}{k}\left(1+\frac{L}{L_m}\right) \tag{25}$$

Table 3 which is the ZVS conditions of all switches considering both output capacitors and magnetizing inductor can be

TABLE 3. ZVS Conditions Considering Output Capacitors and Magnetizing Inductor

Switches	ZVS conditions of mode A	ZVS conditions of mode B
Q_5-Q_8	$D_\varphi \geq \frac{1}{2}\left[1-\frac{1}{k}\left(1+\frac{L}{L_m}\right)\right]$	$D_y \leq \frac{1}{k}\left(1+\frac{L}{L_m}\right)$
Q_3-Q_4	$D_y \geq \frac{2\left(1-D_\varphi\right)+a\sqrt{\left(k^2+2k\right)}}{1+k}$	$\begin{cases} D_y \geq \frac{2D_\varphi + a\sqrt{\left(k^2-2k\right)}}{k-1} & k \geq 2 \\ D_y \geq \frac{2D_\varphi}{k-1} & k < 2 \end{cases}$
Q_1-Q_2	$\begin{cases} D_y \geq \frac{a\sqrt{\left(2k-k^2\right)}-2D_\varphi}{k-1} & k \leq 2 \\ D_y \geq \frac{-2D_\varphi}{k-1} & k > 2 \end{cases}$	$\begin{cases} D_y \geq \frac{a\sqrt{\left(2k-k^2\right)}-2D_\varphi}{k-1} & k \leq 2 \\ D_y \geq \frac{-2D_\varphi}{k-1} & k > 2 \end{cases}$

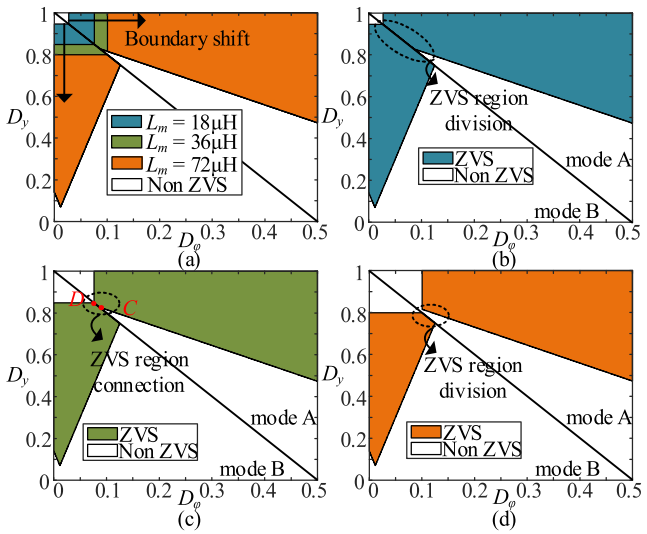

FIGURE 11. ZVS regions of all switches with consideration of 65pF output capacitance and magnetizing inductances. (a) ZVS region comparison. (b) ZVS region with 18 μH magnetizing inductance. (c) ZVS region with 36 μH magnetizing inductance. (d) ZVS region with 72 μH magnetizing inductance.

obtained based on the above analysis. Fig. 11 shows the ZVS regions considering 65pF output capacitance and magnetizing inductances. Fig. 11(a) shows the change trend of ZVS region with the increase of L_m. Fig. 11(b), (c) and (d) show the ZVS regions under the condition of $k = 1.33$ and 65pF output capacitance with consideration of 18 μH, 36 μH and 72 μH magnetizing inductances, respectively.

It can be concluded that the decrease of L_m is useful for connection of ZVS regions. However, a very small L_m has a serious impact on the i_s and the transmission power model. Therefore, the value of L_m should be set reasonably. The ZVS realization constraint condition of L_m is analyzed by using $L_m = 36$ μH for example. As shown in Fig. 11(c), the coordinates of point C and point D are calculated as follows:

$$C: \begin{cases} D_{\varphi\_C} = \frac{1}{2}\left(1-\frac{1}{k}-a\sqrt{1+\frac{2}{k}}\right) \\ D_{y\_C} = \frac{1}{k}+a\sqrt{1+\frac{2}{k}} \end{cases} \tag{26}$$

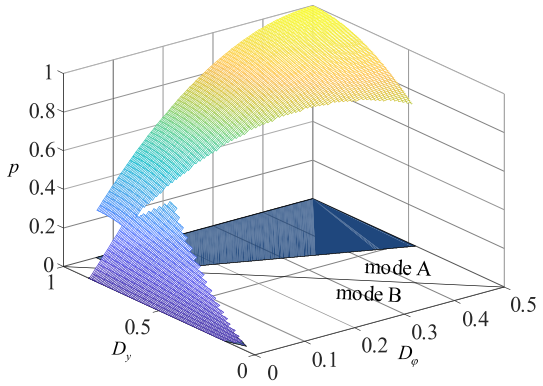

FIGURE 12. Power transfer surface in the ZVS region with 65pF output capacitance and 36 μH magnetizing inductance.

$$D: \begin{cases} D_{\varphi\_D} = \frac{1}{2}\left[1-\frac{1}{k}\left(1+\frac{L}{L_m}\right)\right] \\ D_{y\_D} = \frac{1}{k}\left(1+\frac{L}{L_m}\right) \end{cases} \tag{27}$$

The positions of the two points vary with the magnetizing inductance. To ensure the two parts are connected, the point D should be located at the upper left of the point C. Therefore, the limitation of the magnetizing inductance can be derived as:

$$\begin{cases} \frac{k-\left(1+\frac{L}{L_m}\right)}{2k} \leq \frac{k-1-a\sqrt{k^2+2k}}{2k} \\ \frac{1}{k}+a\sqrt{1+\frac{2}{k}} \leq \frac{1}{k}\left(1+\frac{L}{L_m}\right) \end{cases} \tag{28}$$

Hence, the range of magnetizing inductance is as follows:

$$L_m \leq \frac{L}{a\sqrt{k^2+2k}} \tag{29}$$

The power transfer surface in the ZVS region with 65pF output capacitance and 36 μH magnetizing inductance is shown in Fig. 12. It can be concluded that with the consideration of the magnetizing current, full load range ZVS can be realized. Different combinations of the phase-shift ratios can be selected under soft switching for different transmission power.

IV. ANALYSIS OF THE OPTIMIZATION OF ZVS RANGE AND CURRENT STRESS

Since the conditions of ZVS are inequalities, there are still different combinations of the phase-shift ratios for the same transmission power. Therefore, the phase-shift ratios which satisfy ZVS and minimum current stress simultaneously are analyzed. The normalized values of the current stress in mode A and B are calculated as follows:

$$\begin{cases} I_{1p}^* = 2\left(kD_y + 2D_\varphi - D_y\right) & 0 \leq D_\varphi < \frac{1}{2}\left(1-D_y\right) \\ I_{2p}^* = 2\left(kD_y + 2D_\varphi - D_y\right) & \frac{1}{2}\left(1-D_y\right) \leq D_\varphi < \frac{1}{2} \end{cases} \tag{30}$$

The minimum current stress can be calculated by the Lagrange multiplier method (LMM) and the Karush-Kuhn-Tucker (KKT) conditions. Taking mode A as an example,

the normalized value of the current stress is the optimization goal, the expression of the transmission power is the equality constraint condition, and the unequal relationships of the phase-shift ratios for different modes are the inequality constraint conditions. The KKT conditions can be obtained as:

$$\begin{cases} L = 2\left(kD_y + 2D_\varphi - D_y\right) + \mu_1\left(-D_y\right) + \mu_2\left(D_y - 1\right) \\ +\mu_3\left(1 - D_y - 2D_\varphi\right) + \mu_4\left(2D_\varphi - D_y - 1\right) \\ +\lambda\left(-4D_\varphi^2 - D_y + 4D_\varphi + 2D_y - 1 - p\right) \\ \lambda \neq 0, \quad \mu_1, \mu_2, \mu_3, \mu_4 \geq 0 \\ \frac{\partial L}{\partial D_y} = 0, \quad \frac{\partial L}{\partial D_\varphi} = 0 \\ -4D_\varphi^2 - D_y + 4D_\varphi + 2D_y - 1 - p = 0 \\ \mu_1\left(-D_y\right) = 0, \quad \mu_2\left(D_y - 1\right) = 0 \\ \mu_3\left(1 - D_y - 2D_\varphi\right) = 0, \quad \mu_4\left(2D_\varphi - D_y - 1\right) = 0 \\ \frac{1-D_y}{2} \leq D_\varphi < \frac{1+D_y}{2}, \quad 0 \leq D_y \leq 1 \end{cases} \tag{31}$$

The solution can be calculated as:

$$D_\varphi = \frac{D_y + k - 2}{2\left(k - 1\right)} \tag{32}$$

Furthermore, the range of D_y and the transmission power which satisfies the KKT conditions are as follows:

$$\begin{cases} \frac{1}{k} \leq D_y \leq 1 \\ \frac{2(k-1)}{k^2} \leq p \leq 1 \end{cases} \tag{33}$$

The solution of mode B can be obtained similarly. The relationship of D_φ and D_y in the full power range is as follows:

$$D_y = \begin{cases} 2\left(k - 1\right)D_\varphi + 2 - k & \frac{k-1}{2k} \leq D_\varphi \leq 1 \\ \frac{2D_\varphi}{k-1} & 0 \leq D_\varphi < \frac{k-1}{2k} \end{cases} \tag{34}$$

Based on the expressions of the transmission power and the relationships of D_φ and D_y, the red line on the power transfer surface as shown in Fig. 13(a) can be obtained according to (34), which is the track of phase-shift ratios that represent minimum current stress. Fig. 13(b) shows the D_y - D_φ projection of the curves in Fig. 13(a). As can be seen clearly, part of the control curve is beyond the ZVS region. Under the condition of high switching frequency, we assume that the priority of ZVS is higher than that of the current stress. Therefore, the segment of the control curve which is beyond the ZVS region is compelled to be constrained on the boundary region as shown in Fig. 13(c). So far, the control strategy aiming at optimization of both ZVS range and current stress is determined.

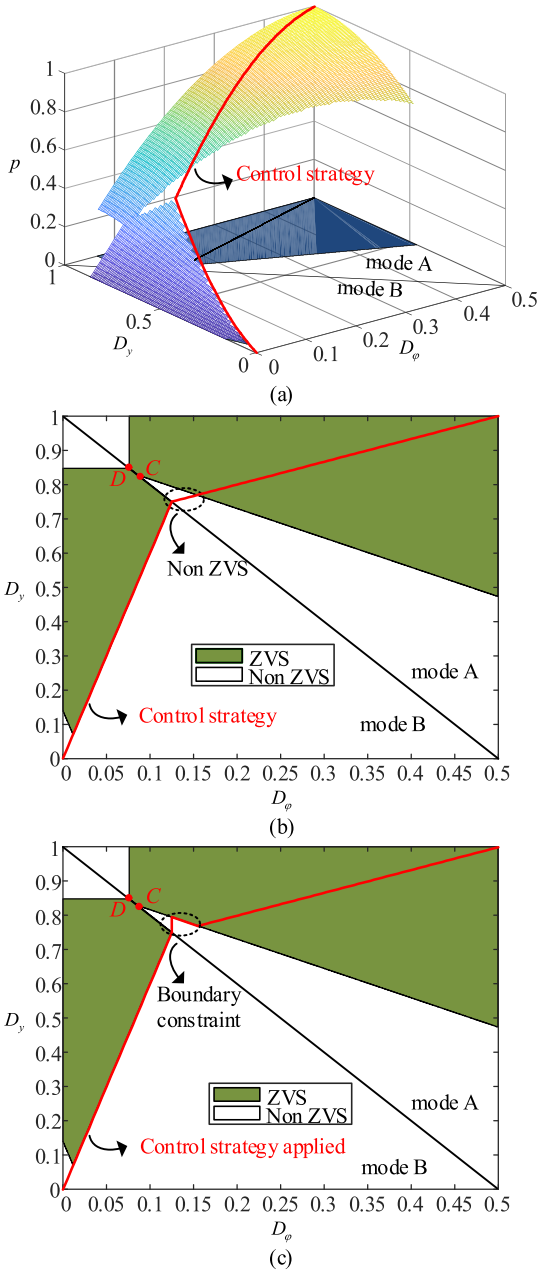

FIGURE 13. Optimization control strategy at case of $k = 1.33$. (a) Control strategy on the power transmission surface. (b) Control strategy in the ZVS region. (c) Applied control strategy in the ZVS region.

V. EXPERIMENTAL RESULTS

To verify the above analysis, a prototype as shown in Fig. 14 with 1kW rated output power and 500kHz switching frequency is built. The dimension of the prototype is 133.2mm (length)×92.7mm (width). The electrical specifications and main used components are summarized in Tables 4 and 5, respectively. The input and output voltages of the system are $V_1 = 400$V and $V_2 = 300$V respectively, which means $V_i = 100$V. The transformer turn ratio is $n = 0.25$. Therefore, voltage conversion ratio is $k = 1.33$.

TABLE 4. Electrical Specifications

Parameters	Value
V_1	400V
V_2	300V
V_i	100V
f	500kHz
k	1.33
Rated Power	1kW

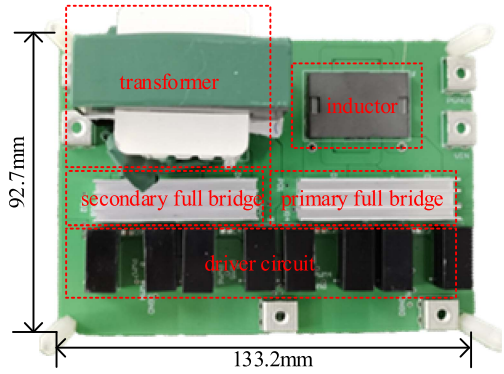

FIGURE 14. Photo of the prototype.

TABLE 5. Main Components Used in Prototype

Components	Model	Parameters
L	E32/6/20	$L = 4.7\mu H$
T	ETD44	$n = 0.25$, $L_m = 36\mu H$
C_1	--	$C_1 = 20\mu F$
C_2	--	$C_2 = 10\mu F$
Q	GS66508B	$C_s = 65pF$

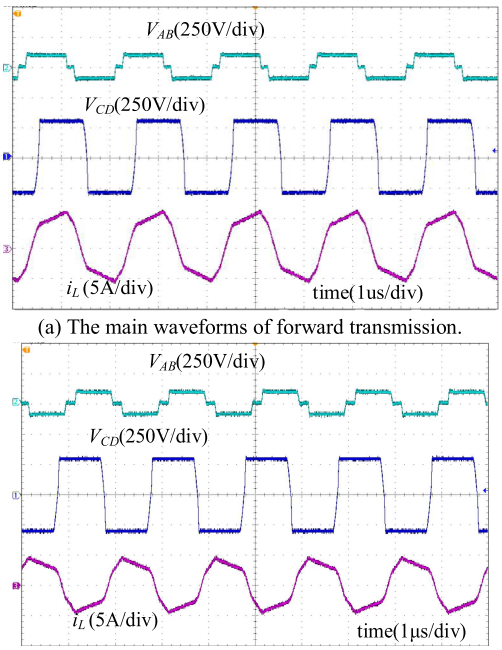

(a) The main waveforms of forward transmission.

(b) The main waveforms of backward transmission.

FIGURE 15. Main waveforms when $p = 0.8$.

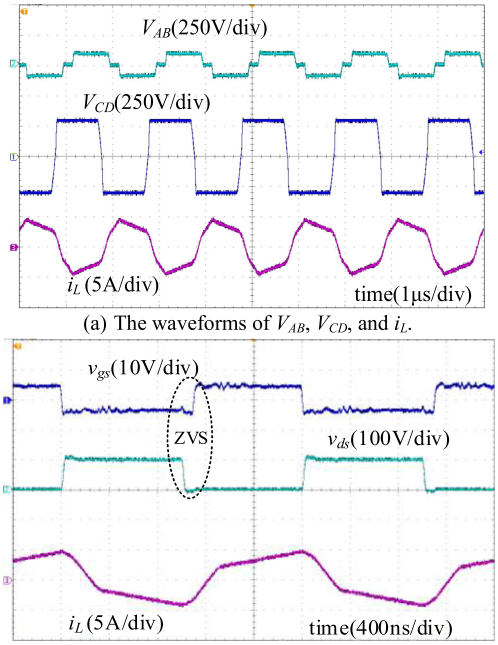

(a) The waveforms of V_{AB}, V_{CD}, and i_L.

(b) The waveforms of Q_1.

FIGURE 16. Main waveforms when $p = 0.6$.

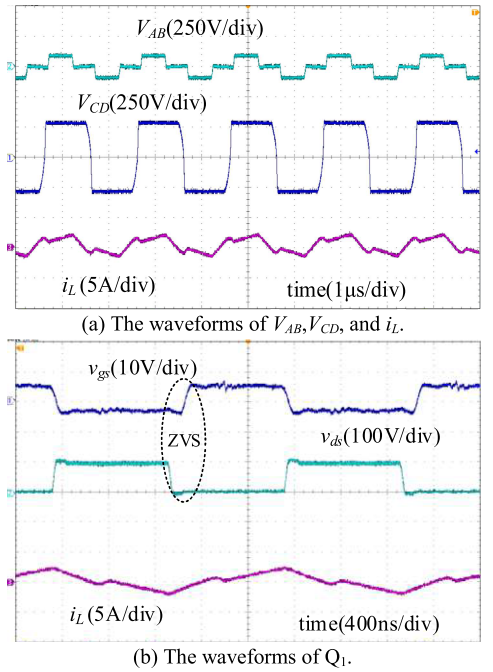

(a) The waveforms of V_{AB},V_{CD}, and i_L.

(b) The waveforms of Q_1.

FIGURE 17. Main waveforms when $p = 0.15$.

Fig. 15(a) and (b) respectively shows the forward and reverse transmission waveforms of V_{AB}, V_{CD} and i_L when $p = 0.8$, which verifies the bidirectional power transmission. It can be seen that the phase relationship of V_{AB} and V_{CD} reverses when the power transmission direction reverses.

Besides the waveforms of V_{AB}, V_{CD} and i_L, Figs. 16(b) and 17(b) show the waveforms of gate-source voltage and drain-source voltage when $p = 0.6$ and 0.15 respectively. As shown in Figs. 16(b) and 17(b), ZVS is realized.

Fig. 18 gives the efficiency curves when $V_2 = 300V$, 320V and 340V, which are shown as red line, green line and blue

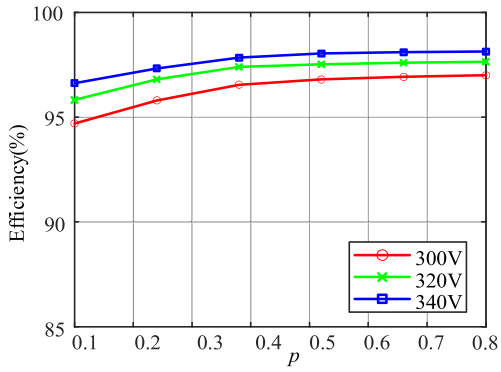

FIGURE 18. Efficiency curves with different output voltage.

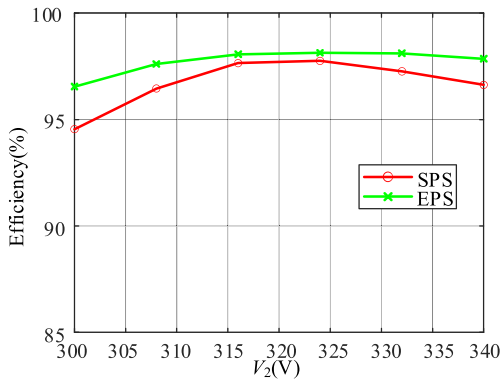

FIGURE 19. Efficiency curves under SPS control and EPS-based control.

line, respectively. As analyzed in Section II, due to the increase the mismatch of the input and output voltages led by the increase of the output voltage, the actual processed power decreases. Therefore, the efficiency becomes higher when the output voltage increases. The peak efficiency under rated output voltage is up to 97.0%.

Fig. 19 shows the efficiency curves under SPS control and the optimal EPS-based control. The power condition of the experiment is $p = 0.4$. The optimal control can ensure the ZVS realization of all switches and minimization of the current stress. Therefore, the efficiency of the converter under optimal EPS-based control is higher than that under SPS control, which is consistent with the analysis.

VI. CONCLUSION

In this article, a DAB-based PPC is adopted. Compared with traditional DAB converters, DAB-based PPCs need a wider voltage regulation range. Therefore, an EPS-based control strategy aiming at optimization of full load range ZVS and minimum current stress is analyzed in detail and applied. For better high frequency performance, the output capacitors are considered and the magnetizing inductor is utilized to solve the separate ZVS region caused by the output capacitors. Finally, a prototype with 1kW rated transmission power and 500kHz switching frequency is built to verify the theoretical analysis. The experimental results are consistent with the analysis and the peak efficiency under rated output voltage is up to 97.0%.

REFERENCE

[1] B. Zhao, Q. Song, W. Liu, and Y. Sun, "Overview of dual-active-bridge isolated bidirectional DC-DC converter for high-frequency-link power-conversion system," *IEEE Trans. Power Electron.*, vol. 29, no. 8, pp. 4091–4106, Aug. 2014.

[2] L. Liu, H. Li, Y. Xue, and W. Liu, "Decoupled active and reactive power control for large-scale grid-connected photovoltaic systems using cascaded modular multilevel converters," *IEEE Trans. Power Electron.*, vol. 30, no. 1, pp. 176–187, Jan. 2015.

[3] D. Das, N. Weise, K. Basu, R. Baranwal, and N. Mohan, "A bidirectional soft-switched DAB-based single-stage three-phase AC–DC converter for V2G application," *IEEE Trans. Transp. Electrific.*, vol. 5, no. 1, pp. 186–199, Mar. 2019.

[4] N. M. L. Tan, T. Abe, and H. Akagi, "Design and performance of a bidirectional isolated DC–DC converter for a battery energy storage system," *IEEE Trans. Power Electron.*, vol. 27, no. 3, pp. 1237–1248, Mar. 2012.

[5] E. L. Carvalho, A. Blinov, A. Chub, P. Emiliani, G. de Carne, and D. Vinnikov, "Grid integration of DC buildings: Standards, requirements and power converter topologies," *IEEE Open J. Power Electron.*, vol. 3, pp. 798–823, 2022.

[6] B. K. Bose, "Power electronics and motor drives recent progress and perspective," *IEEE Trans. Ind. Electron.*, vol. 56, no. 2, pp. 581–588, Feb. 2009.

[7] X. Shen et al., "Adaptive second-order sliding mode control for grid-connected NPC converters with enhanced disturbance rejection," *IEEE Trans. Power Electron.*, vol. 37, no. 1, pp. 206–220, Jan. 2022.

[8] S. A. Q. Mohammed and J.-W. Jung, "A state-of-the-art review on soft-switching techniques for DC–DC, DC–AC, AC–DC, and AC–AC power converters," *IEEE Trans. Ind. Inform.*, vol. 17, no. 10, pp. 6569–6582, Oct. 2021.

[9] G. Xu, D. Sha, Y. Xu, and X. Liao, "Dual-transformer-based DAB converter with wide ZVS range for wide voltage conversion gain application," *IEEE Trans. Ind. Electron.*, vol. 65, no. 4, pp. 3306–3316, Apr. 2018.

[10] B. Zhao, Q. Yu, and W. Sun, "Extended-phase-shift control of isolated bidirectional DC-DC converter for power distribution in microgrid," *IEEE Trans. Power Electron.*, vol. 27, no. 11, pp. 4667–4680, Nov. 2012.

[11] H. Bai and C. Mi, "Eliminate reactive power and increase system efficiency of isolated bidirectional dual-active-bridge DC–DC converters using novel dual-phase-shift control," *IEEE Trans. Power Electron.*, vol. 23, no. 6, pp. 2905–2914, Nov. 2008.

[12] F. Krismer and J. W. Kolar, "Closed form solution for minimum conduction loss modulation of DAB converters," *IEEE Trans. Power Electron.*, vol. 27, no. 1, pp. 174–188, Jan. 2012.

[13] S. S. Muthuraj, V. K. Kanakesh, P. Das, and S. K. Panda, "Triple phase shift control of an LLL tank based bidirectional dual active bridge converter," *IEEE Trans. Power Electron.*, vol. 32, no. 10, pp. 8035–8053, Oct. 2017.

[14] G. Oggier, G. O. García, and A. R. Oliva, "Modulation strategy to operate the dual active bridge DC-DC converter under soft switching in the whole operating range," *IEEE Trans. Power Electron.*, vol. 26, no. 4, pp. 1228–1236, Apr. 2011.

[15] M. Mahdavifard, N. Mazloum, F. Zahin, A. KhakparvarYazdi, A. Abasian, and S. A. Khajehoddin, "An asymmetrical DAB converter modulation and control systems to extend the ZVS range and improve efficiency," *IEEE Trans. Power Electron.*, vol. 37, no. 10, pp. 12774–12792, Oct. 2022.

[16] Q. Gu, L. Yuan, J. Nie, J. Sun, and Z. Zhao, "Current stress minimization of dual-active-bridge DC–DC converter within the whole operating range," *IEEE J. Emerg. Sel. Topics Power Electron.*, vol. 7, no. 1, pp. 129–142, Mar. 2019.

[17] J. Tian, F. Wang, F. Zhuo, Y. Wang, H. Wang, and Y. Li, "A zero-backflow-power EPS control scheme with multiobjective coupled-relationship optimization in DAB-based converter," *IEEE J. Emerg. Sel. Topics Power Electron.*, vol. 10, no. 4, pp. 4128–4145, Aug. 2022.

[18] Y. Tang et al., "Artificial intelligence-aided minimum reactive power control for the DAB converter based on harmonic analysis method," *IEEE Trans. Power Electron.*, vol. 36, no. 9, pp. 9704–9710, Sep. 2021.
[19] A. Taylor, G. Liu, H. Bai, A. Brown, P. M. Johnson, and M. McAmmond, "Multiple-phase-shift control for a dual active bridge to secure zero-voltage switching and enhance light-load performance," *IEEE Trans. Power Electron.*, vol. 33, no. 6, pp. 4584–4588, Jun. 2018.
[20] S. Pistollato, N. Zanatta, T. Caldognetto, and P. Mattavelli, "A low complexity algorithm for efficiency optimization of dual active bridge converters," *IEEE Open J. Power Electron.*, vol. 2, pp. 18–32, 2021.
[21] G. Xu, L. Li, X. Chen, Y. Liu, Y. Sun, and M. Su, "Optimized EPS control to achieve full load range ZVS with seamless transition for dual active bridge converters," *IEEE Trans. Ind. Electron.*, vol. 68, no. 9, pp. 8379–8390, Sep. 2021.
[22] J. Yang et al., "Online digital implementation of wide voltage range RMS-current-optimized control with voltage balancing capability for DAB converter," *IEEE Trans. Power Electron.*, vol. 38, no. 4, pp. 4360–4377, Apr. 2023.
[23] Y. Yan, H. Gui, and H. Bai, "Complete ZVS analysis in dual active bridge," *IEEE Trans. Power Electron.*, vol. 36, no. 2, pp. 1247–1252, Feb. 2021.
[24] J. Tian, F. Wang, F. Zhuo, X. Cui, and D. Yang, "An optimal primary-side duty modulation scheme with minimum peak-to-peak current stress for DAB-based EV applications," *IEEE Trans. Ind. Electron.*, vol. 70, no. 7, pp. 6798–6808, Jul. 2023.
[25] Z. Wang, C. Li, J. Liu, and Z. Zheng, "Influence of output-capacitance and dead-time on dual-active-bridge actual soft-switching-range: Analytic analysis and solution," *IEEE Trans. Power Electron.*, vol. 38, no. 5, pp. 6157–6168, May 2023.
[26] J. Anzola et al., "Review of architectures based on partial power processing for DC-DC applications," *IEEE Access*, vol. 8, pp. 103405–103418, 2020.
[27] M. Kasper, D. Bortis, and J. W. Kolar, "Classification and comparative evaluation of PV panel-integrated DC–DC converter concepts," *IEEE Trans. Power Electron.*, vol. 29, no. 5, pp. 2511–2526, May 2014.
[28] M. S. Agamy et al., "An efficient partial power processing DC/DC converter for distributed PV architectures," *IEEE Trans. Power Electron.*, vol. 29, no. 2, pp. 674–686, Feb. 2014.
[29] S. Rivera et al., "Partial-power converter topology of type II for efficient electric vehicle fast charging," *IEEE J. Emerg. Sel. Topics Power Electron.*, vol. 10, no. 6, pp. 7839–7848, Dec. 2022.
[30] M. C. Mira, Z. Zhang, K. L. Jørgensen, and M. A. E. Andersen, "Fractional charging converter with high efficiency and low cost for electrochemical energy storage devices," *IEEE Trans. Ind. Appl.*, vol. 55, no. 6, pp. 7461–7470, Nov./Dec. 2019.
[31] N. Kim and B. Parkhideh, "PV-battery series inverter architecture: A solar inverter for seamless battery integration with partial-power DC–DC optimizer," *IEEE Trans. Energy Convers.*, vol. 34, no. 1, pp. 478–485, Mar. 2019.
[32] M. Pape and M. Kazerani, "An offshore wind farm with DC collection system featuring differential power processing," *IEEE Trans. Energy Convers.*, vol. 35, no. 1, pp. 222–236, Mar. 2020.
[33] X. Huang, Z. Liu, Q. Li, and F. C. Lee, "Evaluation and application of 600 V GaN HEMT in cascode structure," *IEEE Trans. Power Electron.*, vol. 29, no. 5, pp. 2453–2461, May 2014.
[34] R. Chen and F. F. Wang, "SiC and GaN devices with cryogenic cooling," *IEEE Open J. Power Electron.*, vol. 2, pp. 315–326, 2021.

SHANSHAN GAO (Member, IEEE) was born in Heilongjiang, China, in 1992. She received the B.S., M.S., and Ph.D. degrees in electrical engineering from the Harbin Institute of Technology (HIT), Harbin, China, in 2015, 2017, and 2021, respectively. She is currently an Assistant Professor with the School of Electrical Engineering and Automation, HIT. From 2020 to 2021, she was a Visiting Ph.D. with the Technical University of Denmark, Lyngby, Denmark. Her research interests include high frequency DC-DC converters and LED lighting systems.

YIXUE ZHANG was born in Shanxi Province, China, in 2001. He received the B.S. degree in electrical engineering from the Harbin Institute of Technology, Harbin, China, in 2023. He is currently working toward the M.S. degree. His research focuses on high frequency DC-DC converters.

YIJIE WANG (Senior Member, IEEE) was born in Heilongjiang Province, China, in 1982. He received the B.S., M.S. and Ph.D. degrees in electrical engineering from the Harbin Institute of Technology, Harbin, China, in 2005, 2007, and 2012, respectively. From 2012 to 2014, he was a Lecturer with the Department of Electrical and Electronics Engineering, Harbin Institute of Technology. From 2014 to 2017, he was an Associate Professor with the Department of Electrical and Electronics Engineering, Harbin Institute of Technology. Since 2017, he has been a Professor with the Department of Electrical and Electronics Engineering, Harbin Institute of Technology. His research interests include DC-DC converters, soft-switching power converters, power factor correction circuits, digital control electronic ballasts, LED lighting systems. Dr. Wang is an Associate Editor for IEEE TRANSACTIONS ON INDUSTRIAL ELECTRONICS, IEEE ACCESS, *IET Power Electronics*, and *Journal of Power Electronics*.

JIANXING LIU (Senior Member, IEEE) received the B.S. degree in mechanical engineering and the M.E. degree in control science and engineering from the Harbin Institute of Technology, Harbin, China, in 2004 and 2010, respectively, and the Ph.D. degree in automation from the Technical University of Belfort-Montbeliard, Belfort, France, in 2014. He is currently a Professor with the Department of Control Science and Engineering, Harbin Institute of Technology. His research interests include computational and intelligent systems, sliding mode control, and advanced control techniques for power electronic systems. He is an Associate Editor for several journals, including IEEE TRANSACTIONS ON CIRCUITS AND SYSTEMS II: EXPRESS BRIEFS, IEEE SYSTEMS JOURNAL NONLINEAR DYNAMICS, *ISA Transactions*, and IEEE JOURNAL OF EMERGING AND SELECTED TOPICS IN INDUSTRIAL ELECTRONICS. He is also an Associate Editor for the Conference Editorial Board and IEEE Control Systems Society.

DIANGUO XU (Fellow, IEEE) was born in Heilongjiang, China, in 1960. He received the B.S. degree in control engineering from Harbin Engineering University, Harbin, China, in 1982, and the M.S. and Ph.D. degrees in electrical engineering from the Harbin Institute of Technology (HIT), Harbin, China, in 1984 and 1989, respectively. In 1984, he joined the Department of Electrical Engineering, HIT as an Assistant Professor. Since 1994, he has been a Professor with the Department of Electrical Engineering, HIT. From 2000 to 2010, he was the Dean of School of Electrical Engineering and Automation, HIT. He is also the Vice President of HIT. He has authored or coauthored more than 600 technical papers. His research interests include renewable energy generation technology, power quality mitigation, sensorless vector controlled motor drives, and high performance servo system. Dr. Xu is an Associate Editor for the IEEE TRANSACTIONS ON INDUSTRIAL ELECTRONICS, IEEE TRANSACTIONS ON POWER ELECTRONICS, and IEEE JOURNAL OF EMERGING AND SELECTED TOPICS IN POWER ELECTRONICS. He is the Chairman of IEEE Harbin Section.